AIAA Aviation
22-26 June 2015, Dallas, TX
22nd AIAA Computational Fluid Dynamics Conference

Anisotropic Non-Uniform Block-Based Adaptive Mesh Refinement for Three-Dimensional Inviscid and Viscous Flows

L. Freret* and C. P. T. Groth†
University of Toronto Institute for Aerospace Studies
4925 Dufferin Street, Toronto, Ontario, M3H 5T6, Canada

A parallel anisotropic block-based adaptive mesh refinement (AMR) algorithm is proposed to describe the solution of physically complex flow problems with disparate spatial and temporal scales exhibiting highly anisotropic features on three-dimensional multi-block body-fitted hexahedral meshes with non-uniform grid blocks. Instead of using a classical uniform treatment for the computational cells of each block within the multi-block grids, the proposed anisotropic AMR scheme adopts a non-uniform representation of the cells within each block. With the former approach, all of the cells for a given block are forced to be at the same resolution, including both interior and ghost cells containing solution information from neighboring blocks. In such a uniform representation, various techniques are required to evaluate the solution in the ghost cells and ensure flux conservation at block interfaces with such a uniform representation. The proposed non-uniform approach directly uses the neighboring cells as the ghost cells, even at a grid resolution change, and this affords a number of computational advantages. A modified upwind finite-volume spatial discretization scheme is applied in conjunction with the AMR scheme to the solution of Euler and Navier-Stokes equations for inviscid and viscous compressible gaseous flow. Steady-state and time-varying flow problems are considered on anisotropic adapted meshes. The potential flexibility and efficiency of this enhanced anisotropic AMR scheme are demonstrated for the simulation of flows of varying complexity.

I. Introduction

I.A. Motivation

As computational fluid dynamics (CFD) evolves and its use becomes more widespread in various science and engineering fields, problems involving increasingly complex flow physics often coupled with complicated geometries arise. Typically, these flow problems are difficult to solve due to numerical stiffness arising from the disparate spatial and temporal scales and often require the solution of additional sub-physics equations and/or mathematical models. Specific classes of flows exhibiting these complex features include: *(i)* turbulent flows around complex geometries; *(ii)* chemically reacting flows, especially combustion; *(iii)* electrically conductive flows; and *(iv)* micro-scale flows.

One way to decrease the computational burden when solving complex flow problems without simplifying the physics and maintaining solution accuracy is to use adaptive mesh refinement (AMR). By increasing the number of cells only in those areas of the domain that need to be solved while keeping other areas unchanged, AMR algorithm adapts the mesh for treating the disparate spatial scales without placing extreme demands on computing resources. Parallel block-based AMR[1,2] methods have been proposed previously by Groth and co-workers[3–7] for solving complex flow problems on multi-block body-fitted meshes and applied to the solution of complex flow problems such as non-premixed laminar[4] and turbulent[5] flames as well as turbulent multi-phase rocket core flows,[6] magnetohydrodynamics (MHD) simulations,[3,8] and micron-scale flows.[7] Ivan

*Post-doctoral fellow, lfreret@utias.utoronto.ca
†Professor, Senior Member AIAA, groth@utias.utoronto.ca

et al.[9,10] have also recently applied the block-based AMR techniques to magnetohydrodynamic flows using cube-sphere grids.

The block-based approaches mentioned above were all restricted to isotropic refinement of the mesh, that is, the grid blocks are coarsened or refined equally in all directions. More recently, anisotropic AMR schemes have been investigated in the two-dimensional (2D)[11,12] and three-dimensional (3D)[13,14] cases. What emerged from these studies is that anisotropic AMR can significantly reduce the computational cost in CFD simulations by creating high aspect ratio cells aligned with the regions of the solution that require higher resolution in a preferred direction (e.g., thin layers and shocks) while placing larger cells in regions where the resolution requirements are less stringent. While the previous studies have demonstrated the potential of an anisotropic block-based AMR scheme, they also indicated some key limitations of the methodology, which were adopted in previous both isotropic and anisotropic implementations. In particular, a classical uniform treatment is used to represent the cells, both interior and ghost or halo cells (the latter overlap with neighboring blocks), within a given block at a multi-block grid, regardless of whether or not adjacent grid blocks are at the same level of resolution (refinement). The blocks are extended by a layer of ghost cells while maintaining their refinement level. Standard multigrid type restriction and prolongation operators are required to evaluate the solution in the ghost cells at block resolution changes.[15] Furthermore, a flux correction strategy is required to maintain the flux conservation properties at the solution scheme.[15] While doable for standard second-order schemes in both 2D and 3D meshes, the uniform representation of the cells within each grid block introduces some possible computational inefficiencies. Moreover the additional complications associated with filling the ghost cells and correcting the fluxes would appear to make the implementation of an anisotropic block-based AMR scheme with a high-order spatial discretization method, such as those developed by Ivan et al.[9,16] particularly problematic.

I.B. Scope

In order to avoid the aforementioned difficulties and limitations with uniform grid blocks, an alternative parallel anisotropic block-based AMR scheme is proposed for the solution of physically complex flows exhibiting disparate spatial scales and highly anisotropic features on 3D multi-block body-fitted hexahedral mesh. In the proposed anisotropic AMR scheme, a non-uniform representation is adopted for the cells in each block. This non-uniform representation directly uses the neighboring cells as the ghost cells, even those at different levels of refinement as found at grid resolution changes. This eliminates the need for the restriction and prolongation of solution information and avoids the requirements for conservative flux corrections. The proposed anisotropic AMR scheme would appear to be more tractable and paves the way for the implementation with high-order spatial discretization schemes. In the present paper, the anisotropic block-based AMR scheme with non-uniform grid blocks is applied in conjunction with a second-order finite-volume scheme to the solution of the Euler and Navier-Stokes equations for inviscid and viscous compressible gaseous flows. The remainder of the paper will be organized as follows. The finite-volume scheme and the application of the solution methodology to both steady-state and time-varying problems are described in section II. The extension of the anisotropic AMR to cope with non-uniform cell blocks are discussed in section III. We provide qualitative and quantitative comparisons in sections IV and V to demonstrate the potential of this enhanced anisotropic AMR scheme. The extensions of the anisotropic AMR scheme for use with the high-order finite-volume schemes will be the subject of future follow-on studies.

II. Finite-Volume Scheme

The proposed anisotropic AMR scheme is applied to the solution of Euler and Navier-Stokes equations governing inviscid and viscous compressible three-dimensional flows of a polytropic gas.

II.A. Conservation Forms of the Three-Dimensional Governing Equations

The conservation form of the governing equations for a compressible polytropic gas, either inviscid or viscous, can be written as

$$\frac{\partial \mathbf{U}}{\partial t} + \vec{\nabla} \cdot \vec{\mathbf{F}} = 0, \tag{1}$$

where $\mathbf{U}$ is the vector of conserved solution variables. For a three dimensional Cartesian coordinate system, the Euler equations governing inviscid gaseous flows can be written as

$$\frac{\partial \mathbf{U}}{\partial t} + \frac{\partial \mathbf{F}}{\partial x} + \frac{\partial \mathbf{G}}{\partial y} + \frac{\partial \mathbf{H}}{\partial z} = 0, \tag{2}$$

with

$$\mathbf{U} = \begin{bmatrix} \rho \\ \rho u \\ \rho v \\ \rho w \\ \rho e \end{bmatrix}, \ \mathbf{F} = \begin{bmatrix} \rho u \\ \rho u^2 + p \\ \rho uv \\ \rho uw \\ \rho uh \end{bmatrix}, \ \mathbf{G} = \begin{bmatrix} \rho v \\ \rho uv \\ \rho v^2 + p \\ \rho vw \\ \rho vh \end{bmatrix}, \ \mathbf{H} = \begin{bmatrix} \rho w \\ \rho uw \\ \rho vw \\ \rho w^2 + p \\ \rho wh \end{bmatrix}, \tag{3}$$

where ρ is the gas density, u, v, w are the components of the velocity vector in the x, y, z directions, $e = p/(\rho(\gamma - 1)) + u^2/2$ is the specific total energy, p is the gas pressure and γ is the ratio of specific heats. The vectors $\mathbf{F}$, $\mathbf{G}$, $\mathbf{H}$, are the inviscid flux in the x, y, z directions, respectively such that $\vec{\mathbf{F}} = [\mathbf{F}, \mathbf{G}, \mathbf{H}]$ is the solution flux. The ideal gas equation of state $p = \rho RT$ is used to close the system, where T is the gas temperature and R is the ideal gas constant.

In the case of the Navier-Stokes equations governing viscous gaseous flows, the conservation equations can be expressed as

$$\frac{\partial \mathbf{U}}{\partial t} + \frac{\partial (\mathbf{F} - \mathbf{F_v})}{\partial x} + \frac{\partial (\mathbf{G} - \mathbf{G_v})}{\partial y} + \frac{\partial (\mathbf{H} - \mathbf{H_v})}{\partial z} = 0, \tag{4}$$

where the viscous flux vectors $\mathbf{F_v}, \mathbf{G_v}, \mathbf{H_v}$ in the x, y, and z directions respectively, are given by:

$$\mathbf{F_v} = \begin{bmatrix} 0 \\ \tau_{xx} \\ \tau_{xy} \\ \tau_{xz} \\ -q_x + u\tau_{xx} + \\ v\tau_{xy} + w\tau_{xz} \end{bmatrix}, \ \mathbf{G_v} = \begin{bmatrix} 0 \\ \tau_{xy} \\ \tau_{yy} \\ \tau_{zy} \\ -q_y + u\tau_{xy} + \\ v\tau_{yy} + w\tau_{yz} \end{bmatrix}, \ \mathbf{H_v} = \begin{bmatrix} 0 \\ \tau_{xz} \\ \tau_{yz} \\ \tau_{zz} \\ -q_x + u\tau_{xz} + \\ v\tau_{yz} + w\tau_{zz} \end{bmatrix}. \tag{5}$$

In the preceding equation, q_x, q_y and q_z are the heat flux components and τ_{xx}, τ_{xy}, τ_{xz}, τ_{yy}, τ_{yz}, τ_{zz} are the elements of the fluid stress tensor. As such, the solution flux in (1) is defined by $\vec{\mathbf{F}} = [\mathbf{F} - \mathbf{F_v}, \mathbf{G} - \mathbf{G_v}, \mathbf{H} - \mathbf{H_v}]$.

II.B. Upwind Finite-Volume Scheme for the Governing Equations

The application of a high-resolution upwind finite-volume scheme to the integral form of the conservation equations described in section II.A applied to a hexahedral computational cell (see Figure 1) results in the following semi-discrete form

$$\frac{d\overline{\mathbf{U}}_i}{dt} = -\frac{1}{V_i} \sum_{m=1}^{N_f} \vec{\mathbf{F}}_{i,m} \cdot \vec{n}_{i,m} \, A_{i,m} = -\mathbf{R}_i, \tag{6}$$

where $\overline{\mathbf{U}}_i$ is the average of the conserved solution for the cell i, V_i is the volume of cell i, $\vec{\mathbf{F}}_{i,m}$, $\vec{n}_{i,m}$ and $A_{i,m}$ denote the flux, the outward pointing unit normal and the area of the m^{th} face of cell i, respectively. The integer N_f is the number of faces of the cell and $m \in \{W, E, S, N, B, T\}$ corresponding to the six faces (west, east, south, north, bottom and top) of the cell. The index i corresponds to a cell computational coordinates within a structured mesh. Each structured mesh is contained inside a single block with that block being a part of a multi-block body-fitted mesh with general unstructured connectivity between blocks as shown in Figure 1. Limited linear least-squares solution reconstruction and Riemann-solver based flux functions are used for the evaluation of the numerical flux integrals of (6)[17] . The HLLE or Roe linearized approximate Riemann solver[18] are used in the flux evaluation. The viscous flux evaluation is performed using a Green-Gauss integration over the diamond path to evaluate the gradient at each cell interface.[19]

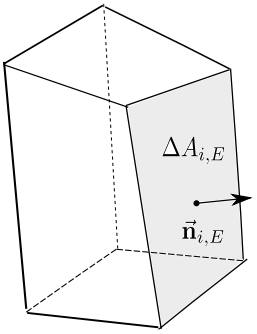

Hexahedral cell i showing face normal vector.

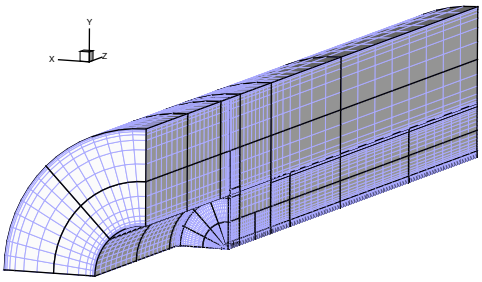

Body-fitted adapted mesh after several refinements. Grid blocks are shown with bold lines

Figure 1. Three-dimensional hexahedral cell (left) and example of mesh (right).

II.C. Explicit Time-Stepping Scheme For Euler Equations

The solution of the semi-discrete form of the Euler equations given in (6) with $\vec{\mathbf{F}} = [\mathbf{F}, \mathbf{G}, \mathbf{H}]$, represented by the area-averaged solution quantities within each computational cell, $\overline{\mathbf{U}}_i$, is obtained herein by applying a standard second-order accurate, Runge-Kutta, explicit time-marching scheme to the resulting coupled non-linear ordinary differential equations (ODEs). Steady-state solutions of the Euler equations are obtained by advancing the solution in time until a converged time-invariant solution is achieved.

II.D. Implicit Time-Stepping Scheme for Navier-Stokes Equations

Newton's method is applied for both steady state relaxation and transient continuation of the Navier-Stokes solution.

$$\mathbf{R}^{\star}(\overline{\mathbf{U}}) = \frac{d\overline{\mathbf{U}}}{dt} + \mathbf{R}(\overline{\mathbf{U}}) = 0. \tag{7}$$

This particular implementation follows the algorithm developed by Groth et al[20, 21] which is well adapted for computations on large multi-processor parallel clusters. This implementation is based on a Jacobian-free inexact Newton method coupled with an iterative Krylov subspace linear solver.

II.D.1. Inexact Newton Method For Steady-State Problems

For steady-state problems, we have

$$\frac{d\overline{\mathbf{U}}}{dt} = \mathbf{R}(\overline{\mathbf{U}}) = 0. \tag{8}$$

The solution of (8) is sought by iteratively solving a sequence of linear systems given an initial estimate $\mathbf{U^0}$. Improved estimates are sucessively obtained by solving

$$\left(\frac{\partial \mathbf{R}}{\partial \overline{\mathbf{U}}}\right)^k \Delta\overline{\mathbf{U}}^k = \mathbf{J}(\overline{\mathbf{U}}^k)\Delta\overline{\mathbf{U}}^k = -\mathbf{R}(\overline{\mathbf{U}}^k), \tag{9}$$

where $\mathbf{J} = \partial\mathbf{R}/\partial\overline{\mathbf{U}}$ is the residual Jacobian. Hence, the improved solution at the k^{th} Newton step iteration is updated with

$$\overline{\mathbf{U}}^{k+1} = \overline{\mathbf{U}}^k + \Delta\overline{\mathbf{U}}^k.$$

Newton iterations are performed until a desired reduction of the residual norm is achieved, that is, $||\mathbf{R}(\overline{\mathbf{U}}^k)|| < \epsilon\ ||\mathbf{R}(\overline{\mathbf{U}}^0)||$. The tolerance ϵ used in this work for steady flows is taken in the range of $[10^{-10}, 10^{-7}]$.
For a system of non-linear equations, each step of Newton's method requires the solution of the linear problem

$$\mathbf{Jx} = \mathbf{b} \tag{10}$$

where $\mathbf{x} = \boldsymbol{\Delta}\overline{\mathbf{U}}$ and $\mathbf{b} = -\mathbf{R}(\overline{\mathbf{U}})$. This large sparse non-symmetric linear system is solved using the generalized minimal residual (GMRES) algorithm of Saad and co-workers.[22] A combination of an additive Schwarz global preconditioner and a block incomplete lower-upper (BILU(2)) local preconditioner is used to speed-up the convergence. As discussed by Dembo et al.[23] providing an exact solution of (10) is not necessary for getting a quick convergence in Newton's method. The convergence tolerance for the iterative solution of the linear problem used in this work is equal to 0.1.

II.D.2. Inexact Newton Method for Unsteady Problems

For unsteady flows, an implicit second-order backward temporal discretization (BDF2) scheme is applied to equation (7) yielding

$$\mathbf{R}^*(\overline{\mathbf{U}}^{n+1}) = \frac{3\overline{\mathbf{U}}^{n+1} - 4\overline{\mathbf{U}}^{n} + \overline{\mathbf{U}}^{n-1}}{2\Delta t} + \mathbf{R}(\overline{\mathbf{U}}^{n+1}) = 0, \tag{11}$$

where Δt is the physical time-step. Application of Newton's method to the solution of (11) leads to the following linear system of equations for the solution update

$$\left[\left(\frac{3}{2\Delta t}\right)\mathbf{I} + \frac{\partial \mathbf{R}}{\partial \overline{\overline{\mathbf{U}}}}\right]\Delta\overline{\mathbf{U}}^{n+1,k} = \mathbf{J}^*\boldsymbol{\Delta}\overline{\mathbf{U}}^{n+1,k} = -\mathbf{R}^*(\overline{\mathbf{U}}^{n+1,k}). \tag{12}$$

In this procedure, at each iteration n, a steady problem is solved using the inexact Newton procedure described in Section II.D.1. The convergence tolerance for the inner iteration loop used here is $\epsilon = 10^{-4}$. The improved approximation for the solution is given by

$$\overline{\mathbf{U}}^{n+1,k+1} = \overline{\mathbf{U}}^{n+1,k} + \Delta\overline{\mathbf{U}}^{n+1,k}.$$

A good initial guess $\overline{\mathbf{U}}^{n+1,k=0}$ consists in using the solution at the previous time step, that is, $\overline{\mathbf{U}}^{n+1,k=0} = \mathbf{U}^n$.

II.D.3. Implicit-Euler Startup For Steady-State Problems

Newton's method can fail if the initial solution estimates fall outside the radius of convergence. For the solution of steady-state problems, an implicit Euler startup procedure of Mulder and Van Leer[24] with successive evolution/relaxation (SER) is used to ensure the global convergence of the method. The application of this startup procedure introducing a low Mach number preconditioning leads to

$$\left[\frac{\boldsymbol{\Gamma}}{\Delta\tau^k} + \left(\frac{\partial \mathbf{R}}{\partial \overline{\overline{\mathbf{U}}}}\right)^k\right]\Delta\overline{\mathbf{U}}^k = -\mathbf{R}^k, \tag{13}$$

where $\boldsymbol{\Gamma}$ is the Weiss-Smith[25] preconditioning matrix for the conserved variables and $\Delta\tau^k$ represents an articifial time-step. As $\Delta\tau^k \to \infty$, Newton's method of Equation (9) is recovered. In the SER approach, the time-step $\Delta\tau$ is varying, starting from a finite-value and gradually increased to become very large as the desired steady solution is approached. As the time step becomes large, Newton convergence is achieved. The time-step size is determined by considering the inviscid Courant-Friedrichs-Lewy (CFL) condition and viscous Von Neumann stability criteria based on the pseudo-compressible system. The maximum permissible time-step for each local cell is determined by

$$\Delta\tau^k \leq \mathrm{CFL}^k \cdot \min\left(\frac{\Delta x}{\max(|\mathbf{u}| + a)}, \frac{\rho\Delta x^2}{\mu}\right),$$

where $\Delta x = V^{1/3}$ is a measure of the grid size and a is the sound speed. The CFL number for the kth iteration is then computed using the following relation

$$\mathrm{CFL}^k = \mathrm{CFL}^0 \frac{||\mathbf{R}(\overline{\mathbf{U}}^{\mathbf{0}})||}{||\mathbf{R}(\overline{\mathbf{U}}^{\mathbf{k}})||}.$$

In this work, we shall consider $\mathrm{CFL}^0 = 100$.

III. Anisotropic Adaptive Mesh Refinement

III.A. Block-Based Adaptive Mesh Refinement

In the block-based AMR scheme, mesh adaptation is accomplished by refining and coarsening pre-defined grid blocks. Each refinement produces new blocks called "children" from a "parent" block and the children can be refined further. A hierarchical tree data structure is used for tracking block connectivity and mesh refinement history.[15] A commonly used strategy to adapt the mesh to key physical features of the flow is to employ indicators based on heuristic measures such the flow gradient. The present work is based on the 3D anisotropic AMR scheme developed by Williamschen and Groth.[13,14] We refer the interested reader to Zhang and Groth[11,12] and Williamschen and Groth[13,14] for a detailed description of the previous implementation in 2D and its extension in 3D, respectively.

III.B. Uniform Block-Based Approach

In the previous implementations of the block-based AMR methods[3–7] as well as in the original isotropic AMR techniques from Gao and Groth,[15] each block contains a structured mesh with $N_i \times N_j \times N_k$ even number of cells and a number of ghost cell layers, N_g, that allow solution information transfer from neighboring blocks. Each block then contains a uniform and structured mesh with $(N_i + 2N_g) \times (N_j + 2N_g) \times (N_k + 2N_g)$ cells. For adjacent grid blocks with resolution changes, this requires prolongation or restriction procedures in one or more directions to fill the neighboring ghost cells. A combination of prolongation and restriction steps may also be required.

Figure 2 shows several of the many possible message passing scenarios. Scenario 1 shows message passing for a resolution change of coarse-to-fine in one direction and the required prolongation in that direction. In scenario 2, restriction in two directions is performed before transferring the solution to the neighbor's ghost cells. Conversely, in scenario 3, prolongation in two directions is performed before transferring the solution to the neighbor's ghost cells. Scenario 4 shows a more complicated message passing for a resolution change of coarse-to-fine in one direction, as well as fine-to-coarse in the another direction. When low-order prolongation (direct injection) is carried out, we automatically have the conservation property

$$\overline{\mathbf{U}}_c A = \overline{\mathbf{U}}_{f_1} A_{f_1} + \overline{\mathbf{U}}_{f_2} A_{f_2},$$

where the subscripts c and f refer to coarse and fine resolution. This condition is generally sufficient for most second-order methods as considered by Williamschen and Groth.[13,14] Unfortunately, this is not the case for high-order schemes where solution reconstruction is required in the coarse cell. This means that the relevant ghost cell solutions should be up-to-date, which is not the case. After only one operation of message passing, ghost cell values are inevitably incorrect. This issue was first identified by Zhang and Groth[12] and was found to have little effect on the solution of steady-state flow problems using explicit iterations, but was found to be detrimental to convergence for implicit iterations and time-accurate simulations. Not allowing cases similar to scenario 4 results in the significantly reduced effectiveness of the anisotropic AMR algorithm. It was found[14] to have the effect of not only increasing local levels of mesh refinement, but also the levels of mesh refinement in neighboring areas in order to maintain refinement level constraints between adjacent blocks. One possible fix for scenario 4 is to iteratively send and receive messages until the error between the values of the interior cells of the neighbor block and the overlapping ghost cells, reduces to an acceptable value as proposed by Zhang and Groth.[12] It was found that 5 iterations of message passing were generally sufficient for fourth-order accuracy. While this was shown to be a acceptable solution[12] for the solution of 2D flows, it adds a layer of unacceptable computational expense for 3D problems and it greatly increases the ratio of inter-block communication to computation. A far more optimal solution is to change the way the block and its ghost cells are defined, so that high-order spatial discretizations can be treated in the same simple and consistent manner as in second-order schemes.

III.C. Non-Uniform Block-Based Approach

In the proposed implementation of anisotropic AMR, the ghost cells are directly provided by the adjacent blocks. All the information (solution and geometry) is used to determine the ghost cells and their solution values. This approach is illustrated in Figure 3, where a 2D representation is used for the sake of clarity. The

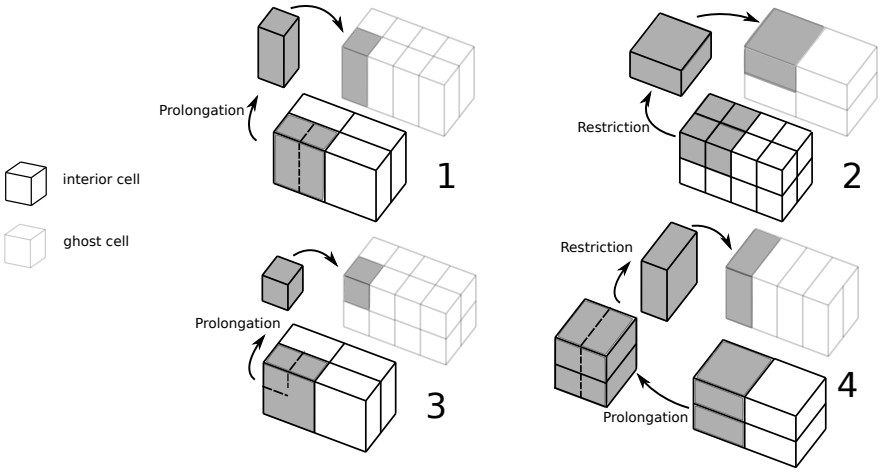

Figure 2. Example of message passing scenarios in anisotropic AMR scheme.

2D grid blocks in Figure 3 are depicted in logical or computational space. In general, the actual grid blocks in physical space can be curvilinear or body-fitted and conform to the geometry of the flow field. Stretching and/or clustering of the gridlines are also permitted. The domain Ω in Figure 3 is decomposed into 11 blocks of (4×8) cells with an anisotropic mesh. On the left-bottom side we represent the uniform structured block geometry provided by the original implementation. It corresponds to the block itself (ID) extended by 2 layers of ghost cells which gives a uniform block mesh of $(4+4) \times (8+4)$ cells. As can be seen, (solution) information belonging to neighboring cells are interpolated to fit the ID's ghost cells. The new non-uniform block is composed of an interior block (ID) enlarged by 2 layers of ghost cells keeping the neighbor's mesh resolution. As shown in Figure 3 (right-bottom), a non-uniform (heterogeneous) block is consisting of 10 sub-elements: the block itself (ID) and 9 block boundary elements (5 edges and 4 corners) arising from the surrounding blocks. In a 3D configuration, the resultant heterogeneous block will contain the interior domain (ID) and at least 26 block boundary elements (6 faces, 12 edges and 8 corners). While a uniform block can be simply represented by one array of values, a non-uniform block is most logically represented by at least 27 arrays of information (solution and geometry). This of course represents an additional layer of complexity; however, it also brings two great advantages. First of all, prolongation and restriction procedures are no longer required to determine the solution content with the ghost cells at grid block resolution changes (we already mentioned that these procedures represent a blocking point in the uniform block representation). In the proposed implementation, ghost cells are directly evaluated by injection from the neighboring block cells. Secondly, it also simplifies the implementation of message passing between adjacent blocks as conservative flux corrections are entirely eliminated by naturally handling the non-conforming cells in the finite-volume method. As a matter of fact, when using uniform blocks, a natural consequence of refining and coarsening is to have non-conforming cells where the faces of both blocks meet. To maintain the conservation properties of the finite-volume scheme, the flux through these non-conforming faces must be corrected. Typical procedures for flux correction involve correcting the solution flux through the coarse cell faces to be equal to that of the total flux through the faces of the cells in the adjacent finer block.[13]

On the other hand, flux evaluation and solution reconstruction procedures for non-uniform blocks become more complicated for cells located at an interior boundary block. In particular, the spatial discretization must allow for the non-uniform nature of the grid and the presence of so-called hanging nodes. These are the tasks of the next section.

III.D. Numerical Flux Evaluation

For a uniform block, the number of faces N_f of each cell in a block is equal to 6, $N_f = \{W, E, S, N, B, T\}$. For a non-uniform block, N_f varies and depends both on the cell position inside the block and the ghost cell mesh refinement. For a cell that is not at a boundary block, $N_f = 6$ since the cells are conforming. For a cell located at a boundary block, $N_f \geq 6$ depending on the geometry of the neighboring blocks. It can take values from $N_f = 6$ (i.e., there is no resolution change) to $N_f = 15$ for a cell located at a block corner with

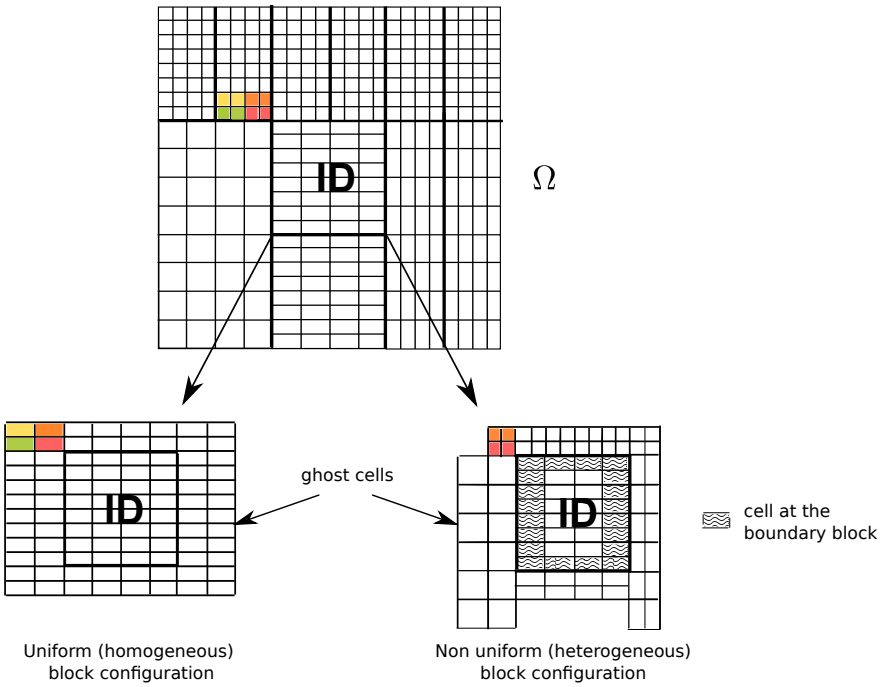

Figure 3. Configuration of a uniform structured mesh block (left-bottom) and non-uniform structured mesh block (right-bottom) from a common block-based anisotropic AMR grid mesh (top).

isotropic changes ($N_f = 3 \times 1 + 3 \times 4 = 15$). These different resolution changes are detailed in Figure 4. For anisotropic AMR, block resolutions in the ξ and η directions are independent, hence this results in 16 different types of resolution changes across block interfaces, which are summarized in the table of Figure 4. Case (a) involves a cell which has an equal or finer mesh than its neighbor ghost cell. In that case all terms of right-hand side in equation (6) are known and can be computed without any additional calculation. Case (b) shows an example of a neighbor ghost cell with a finer mesh. In that case, we do not directly calculate the flux $F_{i,m}$ through the m^{th} face of cell i in equation (6); we consider instead all ghost faces N_g such that $\bigcup_{g \in N_g} A_g = A_{i,m}$. We have

$$\vec{\mathbf{F}}_{i,m} \cdot \vec{n}_{i,m}\, A_{i,m} = -\sum_{g=1}^{N_g} \vec{\mathbf{F}}_{i,m,g} \cdot \vec{n}_g\, A_g, \tag{14}$$

where $\vec{\mathbf{F}}_{i,m,g}$ is the flux through the face A_g. Finally, case (c) involves two cells with two opposite resolution changes in two different directions. For this case, $N_g = 2$ and we consider two new faces such that

$$A_{i,m,g} = \bigcup_{g \in \{1,N_g\}} \left(A_g \cap A_{i,m}\right). \tag{15}$$

We compute the normal vectors $\vec{n}_{i,g}$ of these new faces and finally obtain

$$\vec{\mathbf{F}}_{i,m} \cdot \vec{n}_{i,m}\, A_{i,m} = \sum_{g=1}^{2} \vec{\mathbf{F}}_{i,m,g} \cdot \vec{n}_{i,g}\, A_{i,m,g}. \tag{16}$$

III.E. Solution Reconstruction

A piecewise polynomial approach is used to perform the solution reconstruction within each computational cell of the non-uniform grid blocks, meaning that a solution variable $\mathbf{U}$ in cell i can be represented by

$$\mathbf{U}_i(\vec{X}) = \overline{\mathbf{U}}_i + \mathbf{\Phi}_i \vec{\nabla} \mathbf{U}_i (\vec{X} - \vec{X}_i), \tag{17}$$

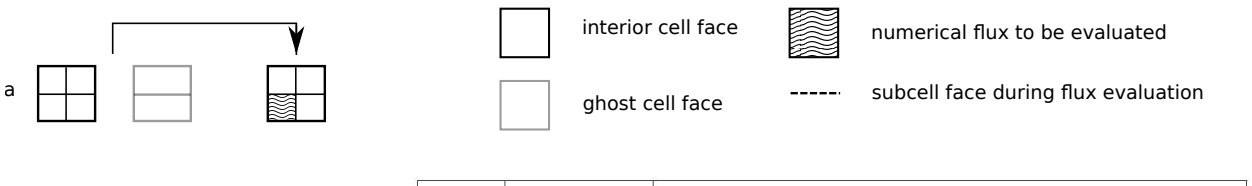

		ID block			
		ξ level η level	ξ level+1 η level	ξ level η level + 1	ξ level + 1 η level + 1
ghost block	ξ level η level	a	a	a	b
	ξ level+1 η level	a	a	c	b
	ξ level η level + 1	a	c	a	b
	ξ level + 1 η level + 1	a	a	a	a

Figure 4. Three scenarios to evaluate the numerical flux through a face of an interior cell depending on its mesh resolution and its neighbor cell mesh resolution.

where $\overline{\mathbf{U}}_i$ is the cell average of the solution at cell i, $\vec{X}_i$ is the centroid of cell i, and $\mathbf{\Phi}_i$ is a slope-limiting function that takes a value between 0 and 1 for each variable to ensure that no new maxima or minima are introduced. The solution gradients $\vec{\nabla}\mathbf{U}_i$ for cell i in (17) can be reconstructed using the N nearest neighbors by a least squares reconstruction that minimizes the third-order accurate error fit

$$\epsilon_i^2 = \sum_{k=1}^{N} \epsilon_{ik}^2 = \sum_{k=1}^{N} \left[\mathbf{U}_k - \mathbf{U}_i - \vec{\nabla}\mathbf{U}_i(\vec{X}_k - \vec{X}_i) - \frac{1}{2}(\vec{X}_k - \vec{X}_i)^T \vec{\nabla}^2 \mathbf{U}_i (\vec{X}_k - \vec{X}_i) \right]^2, \tag{18}$$

where $\vec{\nabla}^2\mathbf{U}_i$ is the Hessian matrix. The minimization of (18) results in a 9×9 system of linear equations which can be solved by a LU decomposition method. This procedure ensures that second-order accuracy is obtained even for non-uniform mesh spacing.

When considering a uniform structured block, we use the neighbors within the first layer around cell i, this corresponds to 26 neighbors in 3D. When dealing with a non-uniform block, the number of neighbors taken into account in (18) is not fixed since it depends on the geometry and mesh topology.

Table 1 finally summarizes the advantages and drawbacks of the two different block structures. When considering non-uniform blocks, routines for restriction/prolongation of the solution as well as flux correction are not required. Since it is directly taken into account in the finite-volume scheme, this implies a simplification of the message passing procedure. On the other hand, the numerical scheme (flux evaluation and solution reconstruction) and the block representation becomes more complicated. This enhanced block-based anisotropic AMR method can handl second-order finite volume scheme as well as high-order numerical scheme at a reasonable cost and efficiency. By contrast, the uniform block-based approach is strictly limited to second-order numerical schemes.

IV. Numerical Results For The Euler Equations

Numerical results for several inviscid flow problems governed by the Euler equations will now be discussed. Results are described for an unsteady three-dimensional shock-cube problem and steady-state supersonic channel flow with a bump. Results using a cubed-sphere mesh[9, 10] are also presented for a steady-state supersonic radial outflow and a steady-state supersonic flow past a sphere. Additionally, an accuracy assessment is performed for this supersonic radial flow problem. The flow problems have been chosen to show the potential of the proposed 3D anisotropic AMR algorithm for significantly reducing computational complexity and to demonstrate the validity of the algorithm for solving both steady-state and time-varying problems. Comparing the results with 3D isotropic AMR illustrates the potential of the AMR scheme in terms of computational cost savings.

Table 1. Pro ans cons of the two different block configurations

	Uniform block	Non-uniform block
restriction / prolongation	yes	no
flux correction	yes	no
message passing procedure	tricky	easy
flux evaluation	easy	tricky
solution reconstruction	easy	tricky
block representation	easy	tricky
second-order method	yes	yes
high-order method	no	yes

IV.A. Unsteady Shock Cube

The shock cube flow problem provides an excellent evaluation of AMR algorithms, requiring high mesh resolution to capture the wave interactions and fast adaptation to the unsteady solution. Due to the highly anisotropic nature of the shock cube solution, it is a good evaluation of 3D anisotropic AMR. The initial conditions for the shock-cube problem are given as standard atmospheric conditions ($\rho = 1.225$ kg/m$^3, p =$ 101325 Pa, $\vec{V} = 0$ m/s, $\gamma = 1.4$) for $x < 0$, $y < 0$, and $z < 0$ and eight times standard atmospheric density and ten times standard atmospheric pressure elsewhere. Reflection boundary conditions are imposed on all boundaries.

Before the simulation begins, the initial mesh with a single block containing $8 \times 8 \times 8$ cells is refined based on the initial conditions six times in order to resolve the discontinuity between the two states and assigned a maximum refinement level of seven. Following the initial refinements, the anisotropic AMR refinement and coarsening procedures are repeated every 15 time-steps until the maximum time $t = 0.75$ ms is reached. The anisotropic adapted grid blocks and solution density contours are plotted at times $t = [0.05, 0.5, 0.75]$ ms in Figure 5. The anisotropic and isotropic density profiles along the diagonal of the domain $[(-0.5, -0.5, -0.5), (0.5, 0.5, 0.5)]$ are also compared.

Throughout the simulation it can be seen that anisotropic AMR tracks the solution well. At $t = 0.05$ ms, there are large anisotropic features in the solution which are exploited by anisotropic AMR using blocks with high aspect ratio cells, resulting in a reduction of 95% in the number of cells compared to that of isotropic AMR. Next the solution begins to move out of alignment with the grid line orientation of the computational blocks, causing anisotropic AMR to produce a more isotropically refined mesh in some regions. Even though the regions for anisotropic refinement are reduced, the anisotropic procedure still offers a mesh size reduction of 58% for $t = 0.5$ ms. At $t = 0.75$ ms, the solution has moved further from alignment with the mesh. Nevertheless, anisotropic refinement still manages to achieve a reduction in the overall size of the mesh of 45%. Moreover, the density profile comparison between isotropic and anisotropic AMR shows a very good agreement between the two approaches.

IV.B. Steady Supersonic Channel Flow Over a Bump

In order to demonstrate the applicability of 3D anisotropic AMR to the solution of steady-state flow problems, supersonic flow over a smooth bump in a channel is studied. This problem consists of a rectangular cross section channel [5.5m×2m×1m] with a smoothed circular bump at the bottom of the channel. Air with a flow Mach number M = 1.4, standard atmospheric density $\rho = 1.225$ kg/m^3 and pressure $p = 101.325$ kPa enters the channel through the left boundary and exits through the right side of the domain. A ratio of specific heats $\gamma = 1.4$ is assumed.

The initial mesh consists of 4 blocks along the length of the channel, 2 blocks along the height of the channel and 1 block along the out of plane direction, each block containing $8 \times 8 \times 2$ cells. Reflection boundary conditions are imposed on the smooth bump boundary and on top of the channel. The flow Mach number M = 1.4 is fixed at the inlet and linear extrapolation is imposed at the outlet. The AMR procedure is limited to a maximum of six refinement levels for each of the computational directions. Steady-state solutions are obtained by advancing the solution in time until a converged time-invariant solution is achieved. The multi-stage optimally smoothing scheme with local time-stepping and CFL equal to 0.5 are used for the temporal

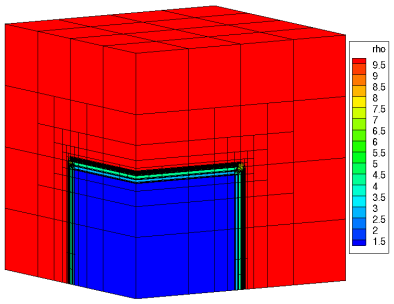

(a) Density field obtained by anisotropic AMR at $t = 0.05\ s$

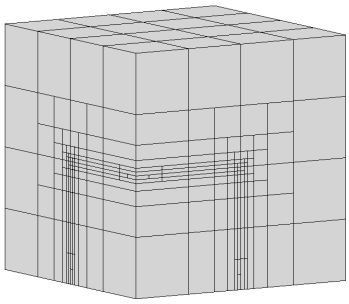

(b) Anisotropic AMR 1080 blocks

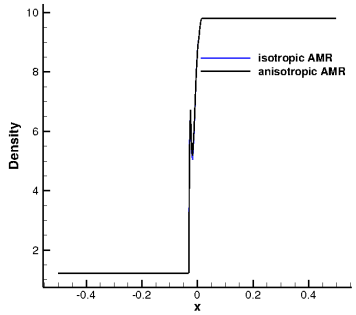

(c) Density profile along a diagonal at $t = 0.05\ s$

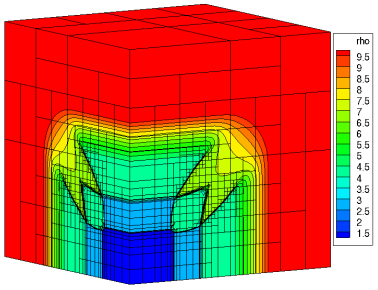

(a) Density field obtained by anisotropic AMR at $t = 0.5\ s$

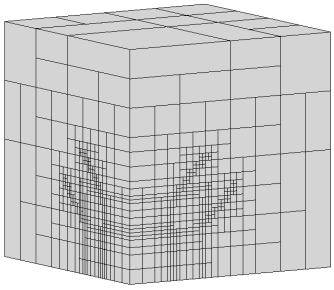

(b) Anisotropic AMR 2941 blocks

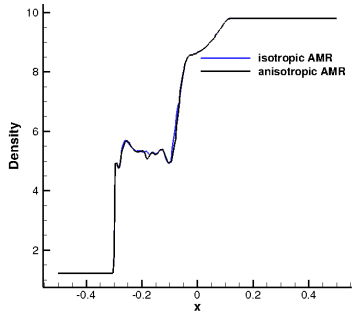

(c) Density profile along a diagonal at $t = 0.5\ s$

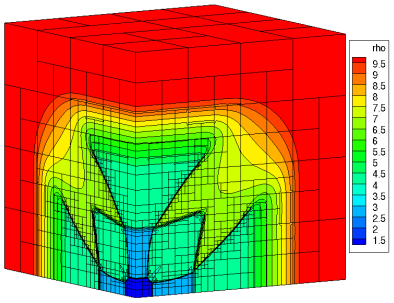

(a) Density field obtained by anisotropic AMR at $t = 0.75\ s$

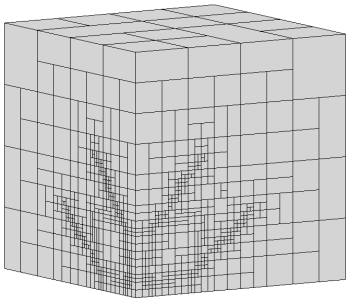

(b) Anisotropic AMR 3347 blocks

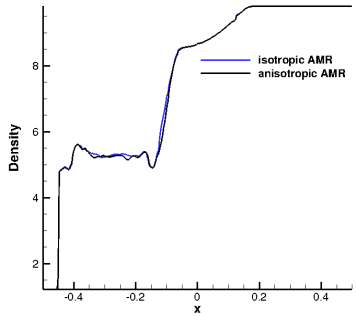

(c) Density profile along a diagonal at $t = 0.75\ s$

Figure 5. Evolution of the gas density field (in kg/m^3 - left) and the blocks (outlined in solid lines - middle) at three different times $t = [0.05, 0.5, 0.75]$. Comparison of the density profile along the cube diagonal $[(-0.5, -0.5, -0.5), (0.5, 0.5, 0.5)]$ between isotropic and anisotropic AMR (right).

integration.

Figure 6 shows the anisotropic block refinement (top) as well as the density field contours (middle). The density profile along $y = 0.25$m is plotted at the bottom of Figure 6 for the isotropic AMR as well as for the anisotropic AMR. We observe an excellent agreement between the two approaches. It is worth mentioning that the number of blocks in the out of plane direction remains equal to one for the anisotropic AMR, which is an expected result considering the two-dimensional feature of the flow. The 3D isotropic AMR requires a huge additional number of cells to achieve a similar spatial resolution, since refinement is necessary in the out of plane direction. A number of 47006 blocks were used for the isotropic AMR simulation while only 1615 blocks were needed for the anisotropic AMR.

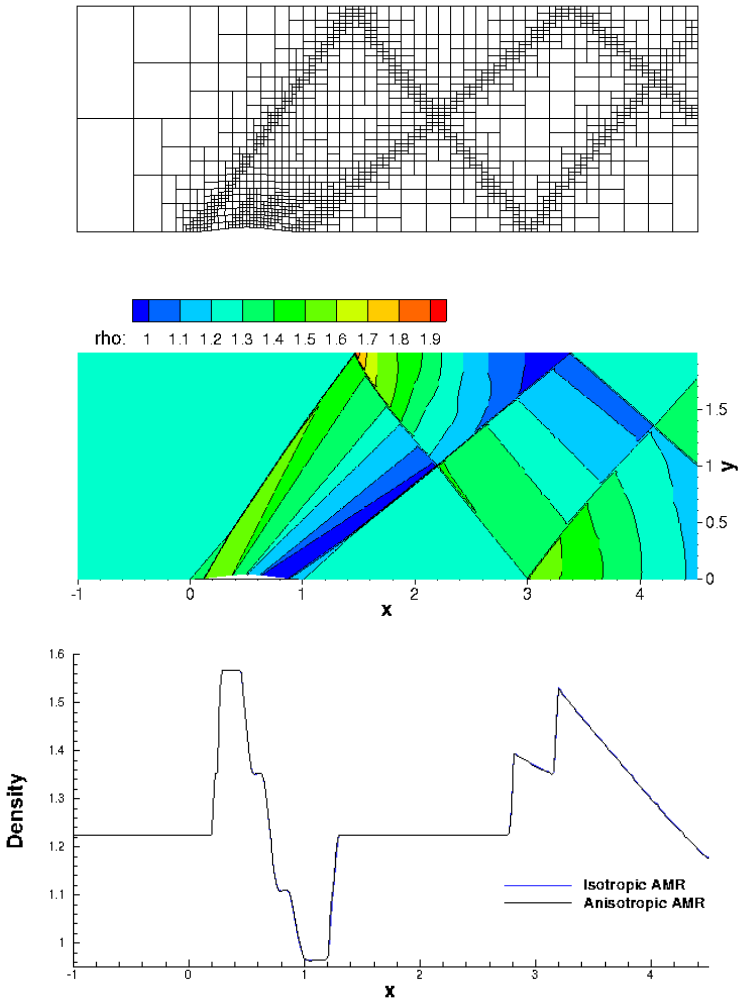

Figure 6. 2D view of a 3D anisotropic mesh (top) used for the solution density contours in kg/m^3 (middle). Density profile obtained by anisotropic AMR and isotropic AMR along the line $y = 0.25m$ (bottom).

IV.C. Steady Supersonic Spherical Outflow

A spherical computational domain is created using the cubed-sphere multi-block mesh from Ivan et al.[9,10] The domain consists of six sectors (or blocks) connected with edges degeneracies, forming an inner hollow sphere and an outer spherical shell. Originally proposed by Ronchi et al.[26] for the solution of partial differential equations in spherical geometries, it has been more recently implemented within the isotropic block-based AMR framework by Ivan et al.[9,10]

As a first investigation into the enhanced non-uniform block-based anisotropic AMR on a cubed-sphere mesh, a simple steady-state flow problem with an analytical solution is examined. In this test-case, we consider a spherical inflow with radius $R_i = 1$ m and a spherical outflow radius of $R_o = 4$ m. Supersonic air enters through the inner sphere with a velocity only in the radial direction (V_r) subsequently expands and exits supersonically through the outflow sphere. The inflow is fixed with flow density $\rho_i = 10$ kg/m^3, radial velocity $V_{r,i} = 4.5$ m/s, and pressure $p_i = 26$ Pa. A ratio of specific heats $\gamma = 1.4$ is assumed. Linear extrapolation is used at the outflow boundary, since the gas is assumed to exit at supersonic speed. The analytical solution to this flow problem which is described by Ivan et al.[9] is taken as the numerical solution

at any radial location (r) to the equation

$$C_3 - \frac{1}{r^2 V_r \left[(C_2 - V_r^2)^{\frac{1}{\gamma-1}} \right]} = 0, \tag{19}$$

where

$$C_3 = \frac{1}{\left(\frac{2\gamma}{\gamma-1} \frac{p_i}{\rho_i}^{\frac{1}{\gamma-1}} \right) R_i^2 V_{r,i}}, \quad C_2 = \frac{2\gamma}{\gamma-1} \frac{p_i}{\rho_i} + V_{r,i}^2, \tag{20}$$

are constants depending on the inflow conditions. The initial mesh consists in a refined cubed-sphere with 24 blocks, each containing $32 \times 32 \times 16$ cells. The integration of the governing equations to machine-zero precision is realized using by the multi-stage optimally smoothing scheme by van Leer et al. with local time-stepping. Six levels of adaptive refinements are completed and the solution is converged at each refinement level.

The predicted flow density obtained using both anisotropic and isotropic AMR at the final level of refinement are depicted on a quarter-slice of the cubed-sphere in Figure 7(a) and 7(b), respectively. It can be observed that the solution varies only along the radial direction and that anisotropic AMR exploits this feature by refining only in the radial direction, while isotropic AMR refines more uniformly. Therefore, a large reduction of 95% in the total cell count compared to isotropic AMR is obtained.

To assess whether this large reduction in the total cell count also corresponds to a significant reduction

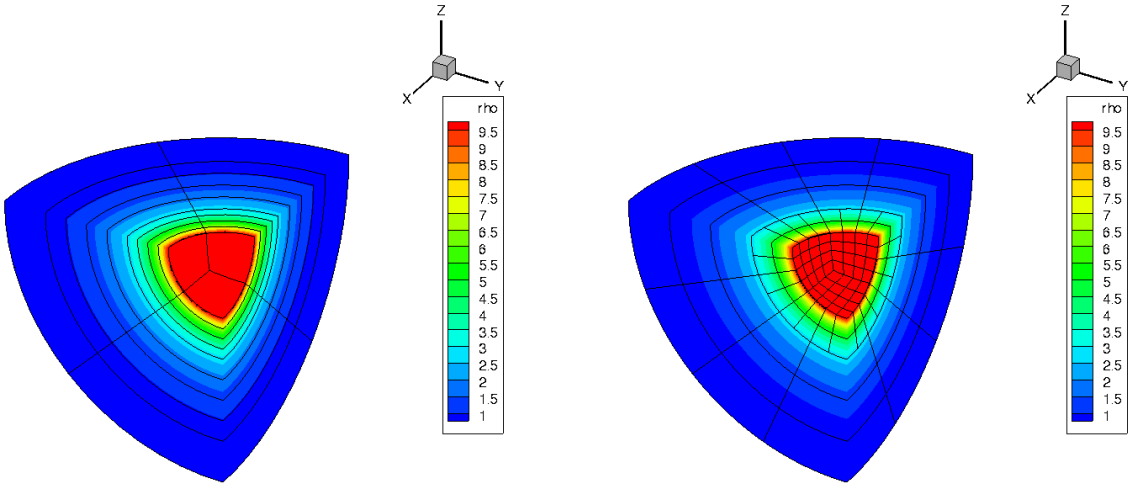

(a) Anisotropic AMR with 54 blocks.

(b) Isotropic AMR with 1056 blocks.

Figure 7. Quarter slices of the predicted solution showing density in kg/m^3 and block outlines for anisotropic and isotropic AMR.

in solution error compared to the isotropic AMR solution, an accuracy estimation has been performed for the supersonic radial outflow problem. After obtaining the converged solution for each refinement level, the solutions are compared to the exact solution given above, and the L_1 and L_2 error norms are computed. The result of this accuracy assessment is shown for anisotropic AMR and isotropic AMR in Figure 8. From the third anisotropic refinement level, the error norms have reached the same level as in the fifth isotropic refined mesh, with just a total block number corresponding to the first isotropic refined mesh, this corresponds to a mesh size saving of 97%.

IV.D. Steady Supersonic Flow Past a Sphere

In this section we consider the solution of a supersonic flow past a sphere. The geometry consists of a half sphere of radius 1 m with a far-field boundary at 10 m as shown in Figure 9. The cubed-sphere mesh for this test-case has only 5 sectors to reduce the problem size and 3 blocks stacked in the radial direction for each sector leading to 15 initial blocks in total with $10 \times 10 \times 10$ cells per block.

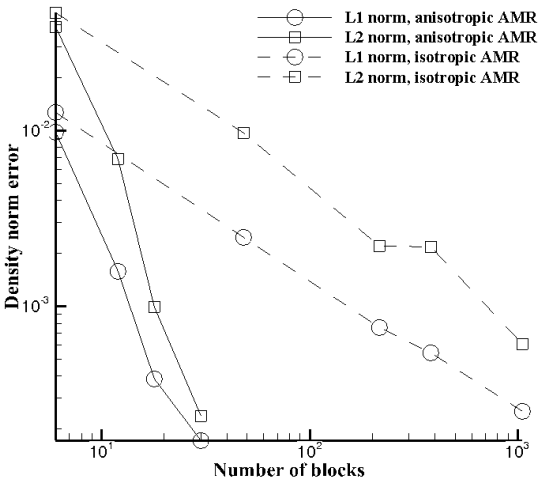

Figure 8. Accuracy assessment based on the exact solution density of the supersonic radial outflow problem comparing anisotropic AMR and isotropic AMR.

Free-stream air with $p = 101.325$ kPa, $\rho = 1.225$ kg/m^3, $M = 2.0$ and $\gamma = 1.4$ enters through the far-field in the positive x direction and exits through the outflow boundary. The far-field boundary condition is fixed at the inflow conditions and the outflow boundary condition is imposed by linear extrapolation since the air exits supersonically. A reflection boundary condition is imposed on the surface of the inner sphere. A multi-stage optimal smoothing scheme with local time-stepping is used for integrating the Euler equations and the HLLE approximate Riemann solver is used for the flux evaluation at cell boundaries.

Figures 10(a) and 10(b) show the solution density and Mach number contours after 5 refinements for anisotropic AMR and isotropic AMR, respectively. In both cases, the adapted mesh is well aligned with the bow shock near the stagnation point and then rapidly loses alignment moving towards the outer regions of the bow shock. Nevertheless, anisotropic AMR still reduces the total number of blocks compared to isotropic AMR by 86% due to the far less refined blocks in the angular directions for anisotropic AMR.

Finally, a comparison of the center line density and Mach number from the stagnation point to the free-stream is given in Figure 11-right. Both methods predict very similar flow field including the shock location and post-shock stagnation conditions.

V. Numerical Results for the Navier-Stokes equations

Next, we present numerical results obtained for the simulation of the Navier-Stokes equations using the implicit time-marching scheme detailed in Section II.D. Three different cases are considered: Steady-state laminar boundary flow past a flat plate (see section V.A), steady-state lid-driven cavity flow (see section V.B) and unsteady Taylor-Green vortex flow (see section V.C). For each case we provide assessments of the computational solutions by comparing the results with analytical solutions or by solving the same problem with isotropic AMR.

V.A. Subsonic Laminar Boundary-Layer Flow Past a Flat Plate

Numerical results for the steady laminar flow over a flat plate are computed and compared with the classical solution of Blasius.[27] The computational domain and boundary conditions are illustrated in Figure 12. A rectangular domain $[-2L, 2L] \times [0, 2L] \times [0, L]$ is used. The far-field and upstream of the plate are modeled by a reflection/slip condition while the presence of the plate, on $x = [0, 2L], y = 0$ is simulated using a no-slip condition. A uniform velocity profile is specified at the inlet ($x = -2L$) and a zero-gradient condition on the fluid velocity is applied at the outlet ($x = 2L$). Pressure is held fixed and equal to 0 at the outlet. The free-stream Mach number and Reynolds number based on the plate length ($L = 0.002$ m) are M_∞=0.2 and

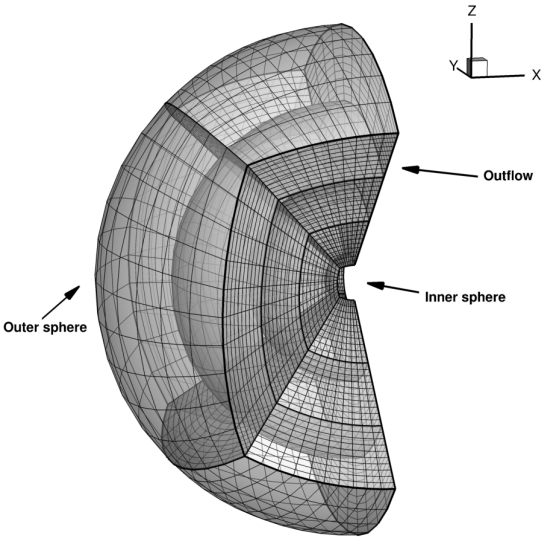

Figure 9. Initial mesh for the steady-state supersonic sphere problem

R_{eL}=9318.92, respectively. The initial condition is a uniform flow of air. The initial mesh consists of 2 blocks of $32 \times 64 \times 2$ cells. Two refinements are performed during the simulation and the solution is converged at each level of refinement.

In Figure 12, the mesh geometry is depicted at the final level of refinement, where 17 blocks are clustered near the leading edge of the plate and near the plate surface. No refinement is performed in the z-direction. The isotropic AMR simulation with the same features would involve 44 blocks. The results are obtained using the inexact Newton's method described in Section II.D.1 for steady flows. Newton iteration are stopped when the non-linear residual is reduced by 10 orders of magnitude ($\epsilon = 10^{-10}$).

In Figure 13-left, the skin friction distribution (C_f) along the flat plate is compared with that of the Blasius analytical solution. Excellent agreement is observed along the entire length of the flat plate. At the exit plane of the flat plate at $x = 0.004$ m, velocity data are extracted across the boundary layer and compared with the Blasius analytical solution. This is shown in Figure 13-right where the velocity profile is plotted using similar variables from the Blasius solution. The predicted non-dimensional boundary layer profiles, u/U_∞ and $\theta = v\sqrt{R_{e_x}/U_\infty}$, are represented at R_{e_x} = 8,900 where U_∞ is the free-stream velocity. Here, the non-dimensional distance from the plate (η) is defined as $y\sqrt{R_{e_x}/x}$. Similarly to skin friction, the velocity profile exhibits excellent agreement with the Blasius solution.

V.B. Lid-Driven Cavity Flow

The proposed solution algorithm is now applied to the well known lid-driven cavity flow problem[28] which demonstrates complex flow physics in a simple geometry with well-defined boundary conditions. Figure 14-left shows a schematic of the cavity-flow geometry. All walls are stationary except for the lid, which is driven at a prescribed velocity, that is,

$$\vec{V} \quad = \quad \begin{cases} \vec{V}_{lid} = (1,0,0) & \text{if } y = 1, \\ \vec{0} & \text{if } x = 0 \text{ or } 1, y = 0, z = 0 \text{ or } 1. \end{cases} \tag{21}$$

The steady laminar flow was computed for a Reynolds number $Re = \rho \, ||\vec{V}_{lid}|| \, L \, / \, \mu = 1000$. The moving wall velocity is equal to 1 m/s and the characteristic length is $L = 1$ m, $\rho = 1$ kg/m^3, $\mu = 10^{-3}$ Pa·s. The Mach number M is small enough such that the solutions obtained for the velocity and pressure fields are very close to those obtained assuming an incompressible flow, $M = 0.1$. Before the simulation begins, the initial mesh with a single block containing $8 \times 8 \times 8$ cells is uniformly refined twice. Two further adaptive refinements are completed and the solution is converged at each refinement level. The mesh adapting criteria are based on both the gradient of density and the gradient of velocity.

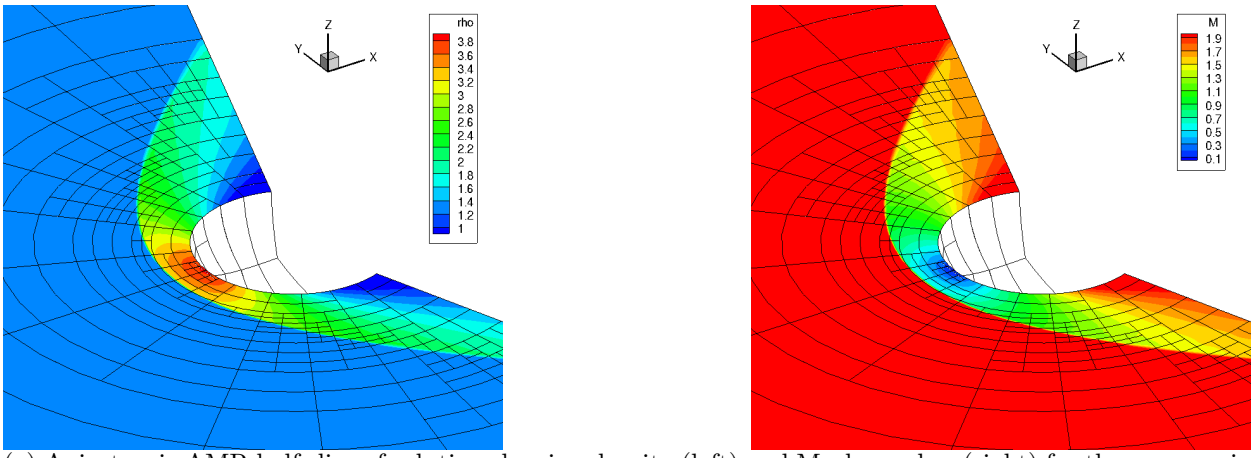

(a) Anisotropic AMR half slice of solution showing density (left) and Mach number (right) for the supersonic sphere problem with 1625 blocks.

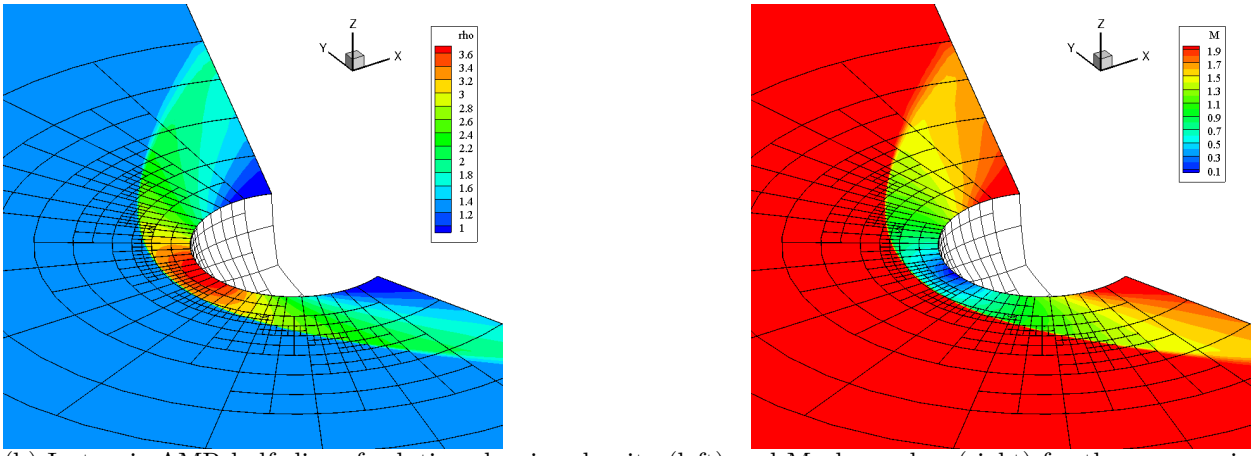

(b) Isotropic AMR half slice of solution showing density (left) and Mach number (right) for the supersonic sphere problem with 12062 blocks

Figure 10. Steady-state $M = 2.0$ sphere problem comparison between anisotropic and isotropic AMR. Blocks are shown outline in black.

The complex recirculating flow pattern arising for this case is depicted at the final level of refinement in Figure 14-right. All the solutions are obtained using the inexact Newton's method described in Section II.D.1 for steady flows. Newton iteration are stopped when the non-linear residual is reduced by 7 orders of magnitude ($\epsilon = 10^{-7}$).

After two adaptive mesh refinements, 764 blocks are used for the anisotropic non-uniform block-based AMR method. The results corresponding to the proposed method are compared with the numerical solution obtained using the isotropic AMR method involving 1639 blocks and the numerical results of Jiang et al.[29] for incompressible flows. The u-velocity profile along a line $x = z = 0.5$ and the v-velocity profile along a line $y = z = 0.5$ are shown in Figure 15. These profiles are in good agreement with the original numerical results.

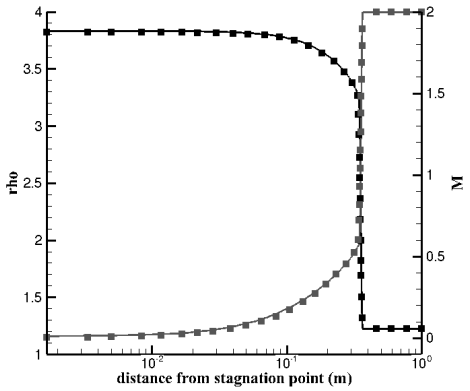

Figure 11. Comparison between 3D anisotropic (lines) and 3D isotropic AMR (symbols) of center line density (black) and Mach number (grey) from the stagnation point to the free-stream.

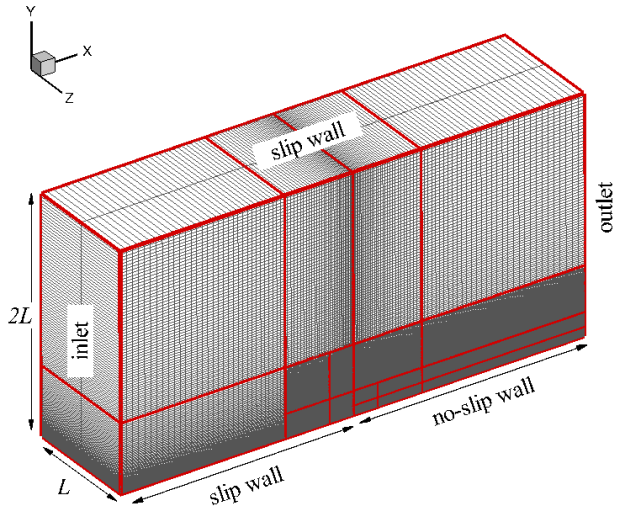

Figure 12. Computational mesh used to study steady laminar flow over a flat plate. The initial mesh consists of 17 blocks of $32 \times 64 \times 2$ cells clustered near the plate surface.

V.C. Taylor-Green Vortex Decay

The Taylor-Green vortex solution[30] is used for testing and validate the spatio-temporal accuracy of the proposed anisotropic AMR for the Navier- Stokes equations. The Taylor-Green vortex solution is given by

$$u = U_0 \ \sin(x)\cos(y)e^{-2\nu t}, \tag{22}$$

$$v = -U_0 \ \cos(x)\sin(y)e^{-2\nu t}, \tag{23}$$

$$w = 0, \tag{24}$$

$$p = p_0 + \frac{\rho_0 U_0^2}{4}[\cos(2x) + \cos(2y)]e^{-4\nu t}, \tag{25}$$

$$\tag{26}$$

over the domain $-\pi \leq x, y, z \leq \pi$, where ν is the kinematic viscosity of the fluid and $\vec{V} = (u, v, w)$ is the velocity vector. Solutions are obtained on a periodic cube domain with length 2π. The initial mesh consists of one block containing $10 \times 10 \times 10$ cells refined four times based on the initial conditions. A sample of computational anisotropic mesh is illustrated in Figure 16-left. The kinematic viscosity, $\nu = \mu_0/\rho_0$, is set to 1.0 m/s^2 with $\rho_0 = 1$ kg/m^3, and the velocity reference is $U_0 = 1$ m/s such that the Reynolds number is $Re = LU_0/\nu = 1$. The initial density field is taken as $\rho = p/(RT_0)$ where T_0 is the initial temperature field.

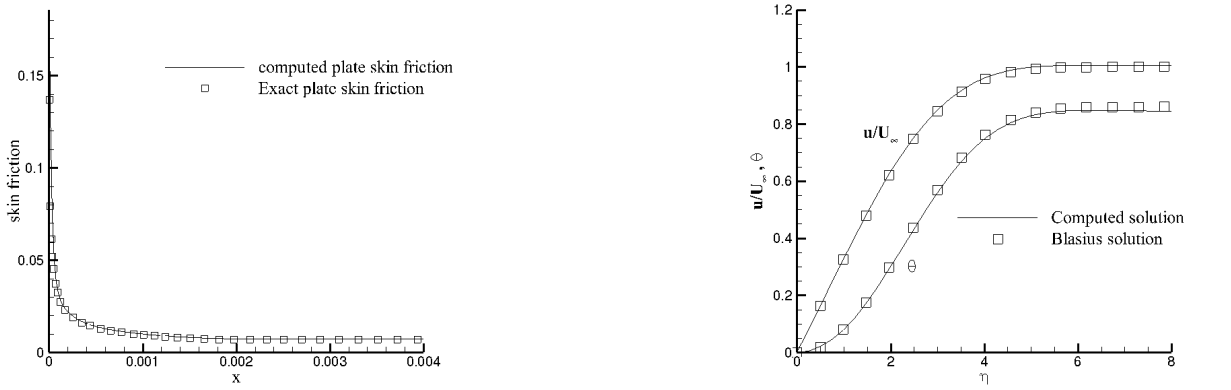

Figure 13. Numerical prediction of subsonic laminar flow, $M = 0.2$ and $Re = 9318.92$ over a 0.0004 flate plate (left) computed plate skin friction (C_f) compared with Blasius solution, (right) non-dimensional velocity profile compared with Blasius solution.

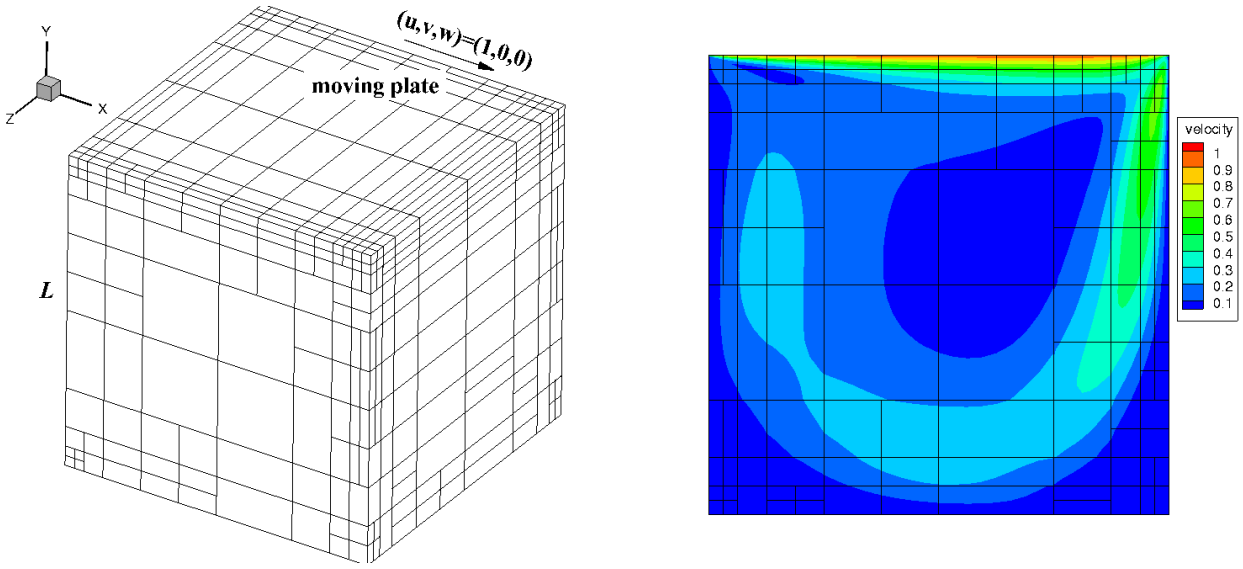

Figure 14. (left) Computational mesh used to study the lid-driven cavity flow with 764 blocks of $8 \times 8 \times 8$ cells, (right) Contours of velocity magnitude, $|\vec{V}|$ along $z = 0.5$ for the lid-driven cavity ($Re = 1000$).

The initial conditions for u in the plane $z = 0$ at time $t = 0$ s is illustrated in Figure 16-left. After 4 successive initial refinements based on the velocity gradient, 160 blocks are used in the anisotropic AMR leading to an efficiency greater than 96%. For the isotropic AMR with the same refinement criteria, 2304 blocks are used with a refinement efficiency of 0.43. As time increases, the magnitude of the velocity exponentially decays through the viscous damping effects. This decay can be seen in Figure16-right which shows the exact solution along $y = z = 0$ at $t = 0.6$ s. Excellent agreement is obtained between the predicted solutions and the exact solution.

VI. Conclusions

A block-based 3D anisotropic AMR using non-uniform grid blocks has been proposed. A description of the new enhanced heterogeneous block and its related numerical resolution have been described in detail. Three-dimensional anisotropic AMR results have been obtained for the Euler equations and for the Navier-Stokes equations. They have been compared to 3D isotropic AMR and analytical solutions to assess the efficiency and accuracy of the proposed approach. Prolongation and restriction of solution and conservative flux

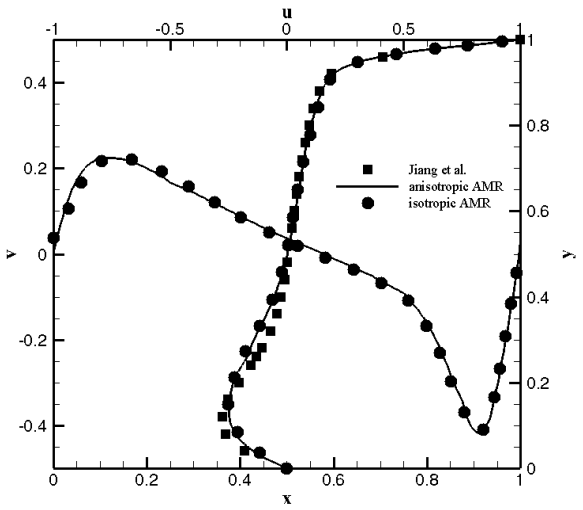

Figure 15. Velocity profiles along centerlines ($y = z = 0.5$ and $x = z = 0.5$) for the lid-driven cavity ($Re = 1000$) for the proposed anisotropic AMR (line), the reference isotropic AMR (circle) and the reference results of Jiang et al.(square).

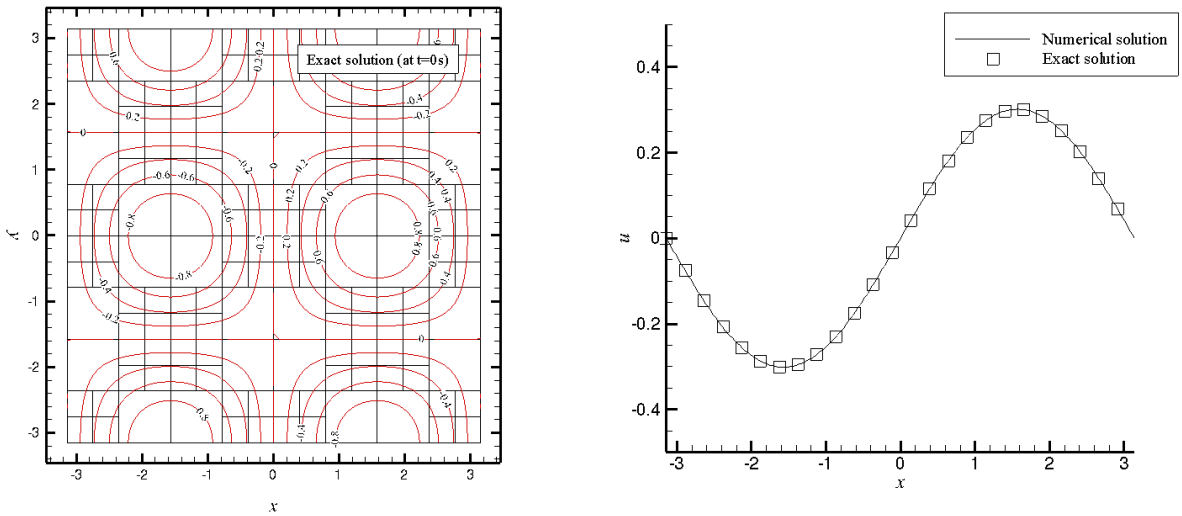

Figure 16. Taylor-Green vortex decay: (left) Initial computational geometry and exact solution for u at $t = 0$s and (right) Solution for u along $y = z = 0$m at $t = 0.6$s.

corrections are avoided as are complexities for high-order solution methods. The potential of the proposed anisotropic AMR method has been demonstrated for a range of 3D test problems governed by Euler and Navier-Stokes equations while offering a significant lower computational complexity and significant reductions in mesh size compared to isotropic AMR techniques.

Acknowledgments

Computational resources for performing all of the calculations reported herein were provided by the SciNet High Performance Computing Consortium at the University of Toronto and Compute/Calcul Canada through funding from the Canada Foundation for Innovation (CFI) and the Province of Ontario, Canada. Additionally, the authors would like to acknowledge the financial support received from the Canadian Space Agency through Space Science and Technology Cluster Pilots Program.

References

[1]M. Berger and J. Saltzman, "AMR on the CM-2," *Applied Numerical Mathematics*, vol. 14, pp. 239–253, 1994.

[2]J. J. Quirk, "A Parallel Adaptive Mesh Refinement Algorithm," tech. rep., NASA, 1993.

[3]C. Groth, D. D. Zeeuw, T. Gombosi, and K. Powell, "Global Three-Dimensional MHD Simulation of a Space Weather Event: CME Formation, Interplanetary Propagation, and and Interaction with the Magnetosphere," *Journal of Geophysical Research*, vol. 105, no. A11, pp. 25,053–25,078, 2000.

[4]S. Northrup and C. Groth, "Solution of laminar diffusion flames using a parallel adaptive mesh refinement algorithm," No. 2005-0547, AIAA, 2005.

[5]X. Gao, *A Parallel Solution-Adaptive Method for Turbulent Non-Premixed Combusting Flows*. PhD thesis, University of Toronto, 2008.

[6]J. Sachdev, C. Groth, and J. Gottlieb, "A parallel solution-adaptive scheme for multi-phase core flows in solid propellant rocket motors," *International Journal of Computational Fluid Dynamics*, vol. 19, no. 2, pp. 159–177, 2005.

[7]J. McDonald and C. Groth, *Numerical modeling of micron-scale flows using the Gaussian moment closure*. University of Toronto, 2005.

[8]C. Groth, D. D. Zeeuw, K. Powell, T. Gombosi, and Q. Stout, "A Parallel Solution-Adaptive Scheme for Ideal Magnetohydrodynamics," 1999.

[9]L. Ivan, H. De Sterck, N. S., and C. Groth, "Multi-dimensional finite-volume scheme for hyperbolic conservation laws on three-dimensional solution-adaptive cubed-sphere grids," *Journal of Computational Physics*, vol. 255, pp. 205–227, 2013.

[10]L. Ivan, H. De Sterck, A. Susanto, and C. Groth, "High-order central eno finite-volume scheme for hyperbolic conservation laws on three-dimensional cubed-sphere grids," *Journal of Computational Physics*, 2015 (to appear).

[11]Z. Zhang and C. Groth, "Parallel high-order anisotropic block-based adaptive mesh refinement finite-volume scheme," 2011.

[12]J. Z. Zhang, "Parallel Anisotropic Block-Based Adaptive Mesh Refinement Finite-Volume Scheme," Master's thesis, University of Toronto, 2011.

[13]M. J. Williamschen and C. P. T. Groth, "Parallel anisotropic block-based adaptive mesh refinement algorithm for three-dimensional flows," in *21th AIAA Computational Fluid Dynamics Conference*, June 2013.

[14]M. Williamschen, "Parallel Anisotropic Block-Based Adaptive Mesh Refinement Algorithm For Three-Dimensional Flows," Master's thesis, University of Toronto, 2013.

[15]X. Gao and C. Groth, "A parallel solution–adaptive method for three-dimensional turbulent non-premixed combusting flows," *Journal of Computational Physics*, vol. 229, no. 9, pp. 3250–3275, 2010.

[16]L. Ivan and C. Groth, "High-order solution-adaptive central essentially non-oscillatory (ceno) method for viscous flows," *Journal of Computational Physics*, vol. 257, pp. 830–862, 2013.

[17]T. Barth, "Recent developments in high order k-exact reconstruction on unstructured meshes," 1993.

[18]P. L. Roe, "Approximate Riemann Solvers, Parameter Vectors, and Diference Schemes"," *Journal of Computational Physics*, vol. 43, pp. 357–372, 1981.

[19]S. A. Northrup, *A parallel implicit adaptive mesh refinement algorithm for predicting unsteady fully-compressible reactive flows*. PhD thesis, University of Toronto, 2013.

[20]C. Groth and S. Northrup, "Parallel implicit adaptive mesh refinement scheme for body-fitted multi-block mesh," in *17th AIAA Computational Fluid Dynamics Conference, Toronto, Ontario, Canada, AIAA paper*, vol. 5333, p. 2005, 2005.

[21]M. Charest, C. Groth, and Ö. Gülder, "Solution of the equation of radiative transfer using a newton-krylov approach and adaptive mesh refinement," *J. Comput. Phys.*, vol. 231, no. 8, pp. 3023–3040, 2012.

[22]Y. Saad and M. Schultz, "Gmres: a generalized minimal residual algorithm for solving nonsymmetric linear systems," *SIAM J. Sci. Stat. Comput.*, vol. 7, no. 3, 1986.

[23]E. S. S. T. Dembo, R.S., "Inexact newton methods," *SIAM, Journal on Numerical Analysis*, vol. 19, 1982.

[24]W. Mulder and B. Van Leer, "Experiments with implicit upwind methods for the euler equations," *Journal of Computational Physics*, vol. 59, pp. 232–246, 1985.

[25]M. J. S. W. Weiss, J.M., "Implicit solution of preconditioned navier-stokes equations using algebraic multigrid," *AIAA Journal*, vol. 37.

[26]R. I. C. Ronchi and P. Paolucci, "The cubed sphere: a new method for the solution of partial differential equations in spherical geometry," *Journal of computational physics*, vol. 124, no. 1, pp. 93–114, 1996.

[27]H. Schlichting, *Boundary-Layer Theory*. McGraw-Hill, Toronto, 1979.

[28]P. Shankar and M. Deshpande, "Fluid mechanics in the driven cavity," *Ann. Rev. Fluid Mech.*, vol. 32, no. 1, pp. 93–136, 2000.

[29]T. P. L. Jiang, B. Lin, "Large-scale computation of incompressible viscous flow by least-squares finite element method," *Computer Methods in Applied Mechanics Engineering*, vol. 144, pp. 213–231, 1994.

[30]G. Taylor and G. A.E., *Mechanism of the production of small eddies from large ones*. Proc. Royal Soc. London, 158(895):499-521, 1937.